

Q-PETR: Quant-aware Position Embedding Transformation for Multi-View 3D Object Detection

Jiangyong Yu¹ Changyong Shu^{1✉} Dawei Yang^{1✉} Zichen Yu²
Xing Hu¹ Yan Chen¹

¹Houmo AI, ²Dalian University of Technology

{jiangyong.yu, changyong.shu, dawei.yang, xing.hu, yan.chen}@houmo.ai
yuzichen@mail.dlut.edu.cn

Abstract

PETR-based methods have dominated benchmarks in 3D perception and are increasingly becoming a key component in modern autonomous driving systems. However, their quantization performance significantly degrades when INT8 inference is required, with a degradation of 58.2% in mAP and 36.9% in NDS on the NuScenes dataset. To address this issue, we propose a quantization-aware position embedding transformation for multi-view 3D object detection, termed Q-PETR. Q-PETR offers a quantization-friendly and deployment-friendly architecture while preserving the original performance of PETR. It substantially narrows the accuracy gap between INT8 and FP32 inference for PETR-series methods. Without bells and whistles, our approach reduces the mAP and NDS drop to within 1% under standard 8-bit per-tensor post-training quantization. Furthermore, our method exceeds the performance of the original PETR in terms of floating-point precision. Extensive experiments across a variety of PETR-series models demonstrate its broad generalization.

1. Introduction

3D perception is crucial for autonomous driving and embodied intelligence [16, 17, 31, 62, 67]. PETR-based methods [29, 30, 43, 49, 50, 52, 56] have gained significant attention due to their effectiveness in this domain. Unlike previous detection methods relying on dense convolutional features [17, 37, 59–61] or utilizing 3D-to-2D projections as in DETR3D-based approaches [25, 28, 51], PETR adapts the paradigm of 2D object detection with transformers (DETR) [5] by incorporating 3D positional encoding, achieving seamless end-to-end 3D obstacle detection.

Despite its advantages, PETR requires substantial storage and computational resources during inference, posing

challenges for on-device deployment. To enhance inference efficiency, considerable efforts have been dedicated to efficient model compression [11, 12, 19, 20, 27, 42], with quantization being particularly favored for deploying models on AI chips by representing networks in low-bit formats [7, 32, 39, 54].

However, deploying complex models like PETR on edge devices presents additional challenges. Autonomous vehicles rely on edge AI chips with limited computational capabilities. Nonlinear functions such as softmax, sigmoid, SiLU, and GeLU are commonly used during inference, but most edge AI chips lack sufficient floating-point performance for these operations, exacerbating deployment difficulties.

Moreover, quantization awareness is often overlooked in neural architecture design, leading to significant performance degradation during deployment. Notably, models like MobileNet [15, 38, 40, 64], EfficientNet [4, 13, 45], and RepVGG [8] face quantization issues requiring additional design efforts or advanced strategies to mitigate deployment challenges. PETR is no exception; when deployed on in-vehicle AI chips, standard 8-bit per-tensor post-training quantization (PTQ) results in a significant performance drop, with a 58.2% decrease in mAP and a 36.9% decrease in NDS.

In this paper, we address the quantization issues of PETR to facilitate its deployment on edge AI chips in autonomous vehicles. We conduct an in-depth analysis of the mechanisms behind PETR’s quantization failure, revealing that the significantly larger magnitudes of positional encodings compared to image features, and the highly imbalanced scaled dot-products in cross-attention, are the primary causes of quantization collapse. Based on these insights, we propose **Q-PETR** (Quantization-aware PETR), a model that mitigates quantization collapse and even improves floating-point performance compared to the original PETR.

Our contributions are summarized as follows:

- **Identifying the root causes of quantization collapse in PETR:** We uncover that the imbalanced output of the inverse-sigmoid function and excessively large values in positional encoding, as well as the imbalanced scaled dot-products in cross-attention, are key issues.
- **Redesigning the positional encoding and quantization strategy:** We reformulate the positional encoding and improve the quantization approach for the scaled dot-product in cross-attention, enhancing both floating-point performance and quantization friendliness.
- **Introducing DuLUT for efficient nonlinear function inference:** We propose DuLUT, an improved lookup table [46] approach that reduces the number of table entries without compromising precision, optimizing nonlinear function inference on edge AI chips.
- **Demonstrating generalizability and deployment readiness:** Our method generalizes well across different model scales, achieving exceptional post-quantization performance suitable for deployment on edge devices.

2. Related Work

3D Object Detection. Surround-view 3D object detection is essential for autonomous driving and is generally categorized into LSS-based [16, 17, 59] and transformer-based [29, 43] approaches. LSS-based methods project multi-camera features onto dense BEV (Bird’s Eye View) representations [37], but their high memory consumption hinders efficient long-range perception. Transformer-based methods leverage sparsity to enhance long-distance perception. Among these, the PETR series has gained significant attention. PETR [29] transforms 2D image features into 3D representations using 3D positional encoding. PETRv2 [30] introduces temporal feature indexing, while StreamPETR [49] extends temporal query processing. Some works [9, 48, 52] accelerate processing by incorporating 2D detection priors. CMT [56] fuses vision and LiDAR point clouds. Improvements to PETR’s positional encoding have also been explored [14, 43]. Additionally, PETR has been integrated into the Omnidrive framework [50] to enhance 3D perception with large models.

Quantization. Quantization compresses models by converting weights and activations from floating-point to lower-bit integer representations [3, 6, 7, 65]. Among various methods [1, 2, 32, 39, 53, 54], we focus on uniform symmetric quantization, mapping floating-point values x_f to discrete k -bit integer values x_q as:

$$x_q = \text{clamp} \left(\left\lfloor \frac{x_f}{s} \right\rfloor, -2^{k-1}, 2^{k-1} - 1 \right), \quad (1)$$

where s is the scaling factor computed as:

$$s = \frac{x_f^{\max} - x_f^{\min}}{2^k}, \quad (2)$$

with x_f^{\max} and x_f^{\min} being the maximum and minimum floating-point values from the calibration dataset. Quantization methods are categorized into Quantization-Aware Training (QAT) and Post-Training Quantization (PTQ). QAT [4, 10] introduces quantization-aware losses during training, enhancing robustness but requiring resource-intensive retraining. PTQ offers rapid deployment without retraining. While PTQ methods have been successful on CNNs [21, 33, 34], they often perform poorly on Vision Transformers (ViTs) and transformer-based detectors due to structural differences. For ViTs, practical PTQ algorithms have been developed [24, 26, 41, 44, 63]. In the context of transformer-based object detection models, Q-DETR [55] and AQ-DETR [47] use QAT and knowledge distillation to mitigate performance degradation in low-bit quantization of DETR models. These methods primarily focus on quantizing GEMM operations. For nonlinear activation functions, lookup table (LUT) techniques [46] are commonly used. Additionally, methods like I-BERT [18] and I-ViT [22] employ integer approximation to achieve fixed-point computation.

Quantization for 3D Object Detection. Quantization methods have been applied to accelerate 3D object detection in autonomous driving and robotics. Leveraging advances in image quantization, QD-BEV [66] employs QAT and distillation in multi-camera 3D detection, achieving smaller models and faster inference than the *BEVFormer* baseline [23]. For LiDAR-based detection, LIDAR-PTQ [68] achieves state-of-the-art quantization on *CenterPoint* [58], with performance close to FP32 and a threefold speedup. To our knowledge, no PTQ solution currently exists for transformer-based 3D object detection in autonomous driving.

3. Quantization and Deployment-Friendly Adaptation of PETR

In this section, we aim to improve PETR’s quantization performance. We begin by introducing the principles of PETR (§3.1), identify its quantization failures (§3.2), and provide strategies to address these challenges (§3.3).

3.1. Preliminaries

PETR enhances 2D image features with 3D position-aware properties using camera-ray positional encoding (PE), enabling refined query updates for 3D bounding box prediction. Specifically, surround-view images \mathbf{I} pass through a backbone to generate 2D features \mathbf{f}_{2D} , while camera-ray PE p_c is computed using camera intrinsics and extrinsics. The learnable query embeddings q serve as the initial queries \mathbf{Q} for the decoder. Here, \mathbf{f}_{2D} serves as the values \mathbf{V} , and adding p_c to \mathbf{f}_{2D} element-wise forms the 3D position-aware keys \mathbf{K} .

The decoder updates the queries using these key-value pairs through self-attention, cross-attention, and feed-forward network (FFN) modules. The updated query vectors are passed through an MLP to predict 3D bounding box categories and attributes, repeating for L cycles. The entire PETR process is summarized in Algorithm 1.

Algorithm 1: Pseudo-code of PETR.

Data: Surround-view images \mathbf{I} , camera intrinsics and extrinsics
Result: 3D bounding boxes \mathbf{b}^l , categories \mathbf{c}^l for $l = 1$ to L

- 1 Compute image features: $\mathbf{f}2D = \text{Backbone}(\mathbf{I})$; Compute camera-ray PE p_c using camera intrinsics and extrinsics; Form 3D position-aware keys: $\mathbf{K} = \mathbf{f}2D + p_c$
// Element-wise addition
- 2 Set values: $\mathbf{V} = \mathbf{f}2D$; Initialize queries: $\mathbf{Q} = q$; **for** $l = 1$ to L
do
- 3 $\mathbf{Q} \leftarrow \text{QProj}(\mathbf{Q})$; $\mathbf{K} \leftarrow \text{KProj}(\mathbf{K})$; $\mathbf{V} \leftarrow \text{VProj}(\mathbf{V})$;
 $\mathbf{A}_s = \text{MultiHeadAtt}(\mathbf{Q}, \mathbf{Q}, \mathbf{Q})$
// Self-attention
- 4 $\mathbf{A}_c = \text{MultiHeadAtt}(\mathbf{A}_s, \mathbf{K}, \mathbf{V})$
// Cross-attention
- 5 $\mathbf{Q} \leftarrow \text{FFN}(\mathbf{Q} + \mathbf{A}_c)$; $\mathbf{b}^{l+1} \leftarrow \text{MLP}(\mathbf{Q})$;
 $\mathbf{c}^{l+1} \leftarrow \text{MLP}(\mathbf{Q})$;
- 6 **end**
- 7 **return** $\mathbf{b}^l, \mathbf{c}^l$ for $l = 1$ to L ;

3.2. Quantization Failure of PETR

We evaluate the performance of several PETR configurations [29] using the official code. Under standard 8-bit symmetric per-tensor post-training quantization (PTQ), PETR suffers significant performance degradation, with an average drop of 58.2% in mAP and 36.9% in NDS on the nuScenes validation dataset (see Table 1).

Bac	Size	Feat	FP32 Acc		INT8 Acc	
			mAP	NDS	mAP	NDS
R50	1408×512	c5	30.5	35.0	18.4(12.1↓)	27.3(7.7↓)
R50	1408×512	p4	31.7	36.7	15.7(16.0↓)	26.1(10.6↓)
V2-99	800×320	p4	37.8	42.6	10.9(26.9↓)	23.6(19.0↓)
V2-99	1600×640	p4	40.4	45.5	11.3(29.1↓)	23.9(21.6↓)

Table 1. PETR’s performance of 3D object detection on nuScenes val set, directly utilizing the pre-trained parameters from the official repository.

Layer-wise Quantization Error Analysis. Quantizing a pre-trained network introduces output noise, degrading performance. To identify the root causes of quantization failure, we employ the signal-to-quantization-noise ratio (SQNR), inspired by recent PTQ advancements [35, 36, 57]:

$$SQNR_{q,b} = 10 \log_{10} \left(\frac{\sum_{i=1}^N \mathbb{E}[\mathcal{F}\theta(x_i)^2]}{\sum_{i=1}^N \mathbb{E}[e(x_i)^2]} \right) \quad (3)$$

Here, N is the number of calibration data points; $\mathcal{F}\theta$ denotes the full-precision network; the quantization error is $e(x_i) = \mathcal{F}\theta(x_i) - \mathcal{Q}_{q,b}(\mathcal{F}\theta(x_i))$; and $\mathcal{Q}_{q,b}(\mathcal{F}\theta)$ represents the network output with quantization applied at bit-width b , while other layers remain at full precision.

Since 8-bit weight quantization incurs minimal information loss, we focus on quantization errors related to operator inputs. Using the PETR configuration from the first row of Table 1, we obtain layer-wise SQNRs, depicted in Fig. 1. From these results, we identify three primary observations contributing to quantization errors:

Observation 1: The inverse-sigmoid operator disrupts feature distribution balance. As indicated by the red arrow in Fig.1, quantization difficulties stem from PETR’s positional encoding module. Analyzing its construction (Fig.5(a)), we find that the inverse-sigmoid operation induces an imbalanced feature distribution. Specifically, Fig. 2 shows that before applying inverse-sigmoid, the feature distribution is balanced and quantization-friendly, whereas afterward, it exhibits significant outliers. Thus, avoiding the inverse-sigmoid operator in the positional encoder is advisable.

Observation 2: Disparity in magnitude between camera-ray PE and image features leads to information loss after quantization. The issue highlighted by the purple arrows in Fig.1 indicates that applying 8-bit symmetric linear quantization to the 3D position-aware key \mathbf{K} significantly degrades performance. Since \mathbf{K} is derived by element-wise summing image features and camera-ray PE, we quantize them using \mathbf{K} ’s quantization parameters, as visualized in Fig.3. Clearly, image features occupy only 4 bits, causing severe information loss. Designing a positional encoding with a magnitude distribution similar to image features is crucial to address this quantization issue.

Observation 3: The scaled dot-product in cross-attention exhibits significant fluctuations along the head dimension. As highlighted by the green arrow in Fig.1, the scaled dot-product in cross-attention presents quantization challenges. Since the subsequent softmax operation is applied along the last dimension, we visualize the maximum values over this dimension in Fig.4. The feature distribution varies significantly across different heads, posing challenges for effective per-tensor quantization.

3.3. Quantization and Deployment Friendly Improvement.

Based on the analysis in Section 3.2, we identify two key areas for improvement: (1) designing a positional encoding with magnitude and distribution similar to image features, and (2) balancing the scaled dot-products in cross-attention across heads. We propose specific methods to address these challenges.

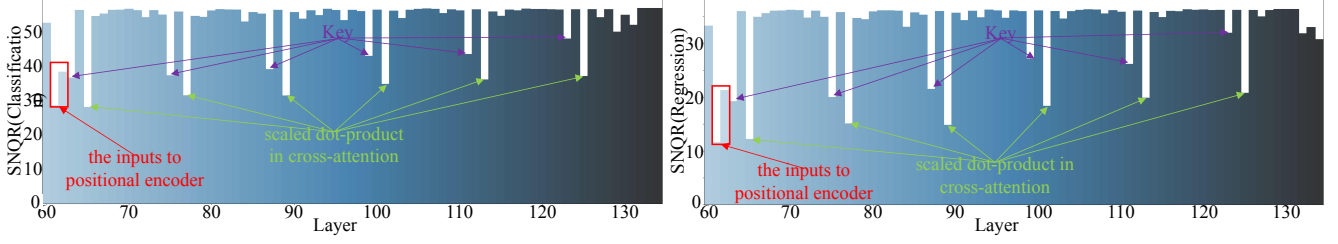


Figure 1. The layer-wise SNQR for classification and regression respectively. For clarity in the illustration, the layers in backbone are omitted, as its quantization does not cause any performance degradation

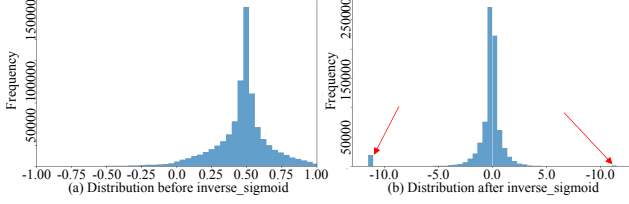


Figure 2. Feature distribution before and after the inverse-sigmoid operator. Red arrows highlight outliers.

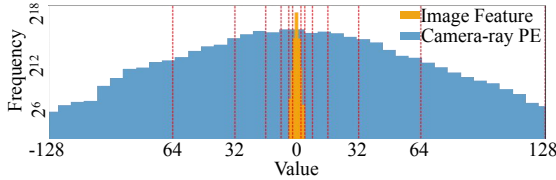


Figure 3. The distributions of image features and camera-ray position encodings after symmetric quantization using the quantization parameters derived from the 3D position-aware \mathbf{K} .

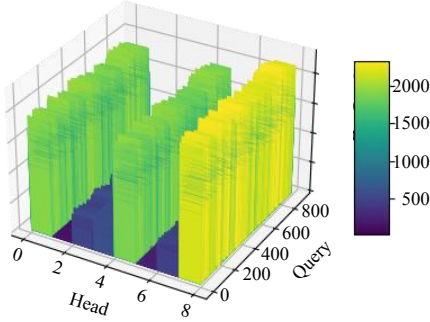


Figure 4. The distributions of scaled dot-product in cross-attention. There are significant amplitude fluctuations along the head dimension.

Positional Encoding Adaptation. To reduce the magnitude of positional encoding in PETR, we analyze its construction process (Fig.5(a)). PETR samples 64 3D points along each camera ray per pixel, increasing magnitude variance. According to statistical theory, the variance of a sum increases with the number of variables. Inspired by 3DPPE [43], which introduces a lidar-centered lidar-ray PE

using only one 3D point (Fig.5(b)), we design a quantization and deployment-friendly (QD-aware) lidar-ray PE (Fig.5(c)).

Our QD-aware lidar-ray PE avoids both the inverse-sigmoid operator and sinusoidal calculations, making it suitable for quantization and deployment on edge devices. Specifically, we learn three anchor embeddings along each axis $\alpha \in x, y, z$, denoted E_α^i with anchor locations L_α^i for $i = 1, 2, 3$. For each lidar-ray point (x_j, y_j, z_j) , we identify the two closest anchors and compute interpolated embeddings:

$$\begin{aligned}
 e_x^j &= \frac{x_j - L_x^{i_x}}{L_x^{i_x+1} - L_x^{i_x}} E_x^{i_x+1} + \frac{L_x^{i_x+1} - x_j}{L_x^{i_x+1} - L_x^{i_x}} E_x^{i_x}, \\
 e_y^j &= \frac{y_j - L_y^{i_y}}{L_y^{i_y+1} - L_y^{i_y}} E_y^{i_y+1} + \frac{L_y^{i_y+1} - y_j}{L_y^{i_y+1} - L_y^{i_y}} E_y^{i_y}, \\
 e_z^j &= \frac{z_j - L_z^{i_z}}{L_z^{i_z+1} - L_z^{i_z}} E_z^{i_z+1} + \frac{L_z^{i_z+1} - z_j}{L_z^{i_z+1} - L_z^{i_z}} E_z^{i_z}.
 \end{aligned} \quad (4)$$

The QD-aware lidar-ray PE is then obtained via $MLP([e_x^j, e_y^j, e_z^j])$, where $[\cdot]$ denotes concatenation along the channel dimension, and the MLP has a conv-relu-conv structure.

Quantization Strategy for Scaled Dot-Product in Cross-Attention. In softmax operations, numerical stabilization (NS) subtracts the maximum value to prevent overflow. Traditional quantization quantizes before NS, leading to issues in **Observation3**. We propose quantizing after NS (Fig.6), and adaptively determining the optimal truncation lower bound to minimize softmax error.

After NS, inputs to softmax are non-positive. Values below -20 approach zero after exponentiation, so we define a candidate set of scaling factors $S = s_1, s_2, \dots, s_N$ with $s_i = \frac{i}{2^{k-1}}$ for k -bit quantization. The dequantized input \hat{x}_s^i is:

$$\hat{x}_s^i = s_i \cdot \text{clamp} \left(\text{round} \left(\frac{x_s}{s_i} \right), -2^{k-1}, 2^{k-1} - 1 \right), \quad (5)$$

ensuring $\hat{x}_s^i \in [-i, 0]$. We compute the softmax distributions $p_f = \text{softmax}(x_s)$ and $p_q^i = \text{softmax}(\hat{x}_s^i)$, and select

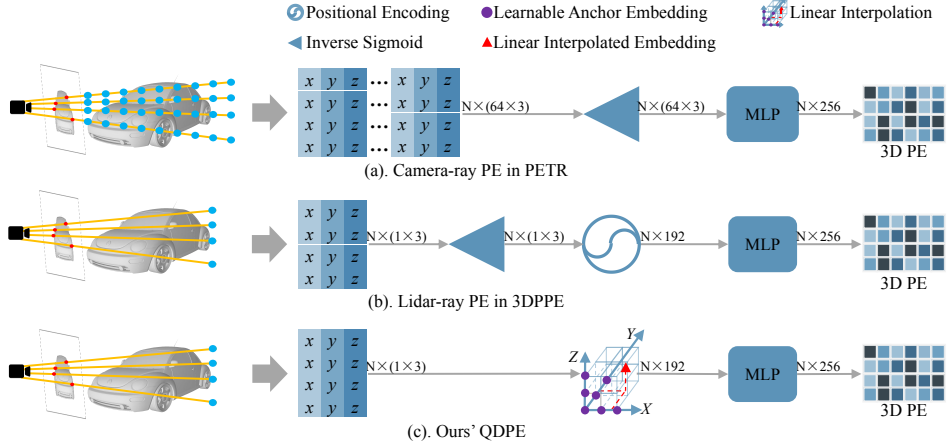


Figure 5. The overall architecture comparison of camera-ray PE, lidar-ray PE and our QD-aware lidar-ray PE.

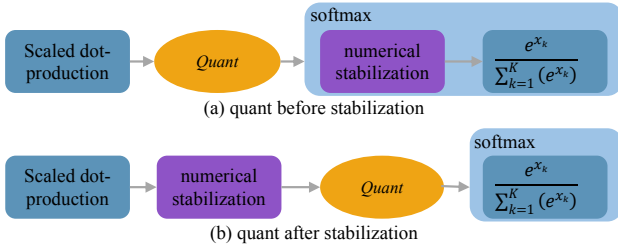


Figure 6. Illustration for quant before/after stabilization.

the optimal scaling factor \hat{s}_i minimizing the error:

$$\hat{s}_i = \underset{i}{\operatorname{argmin}} |p_f - p_q^i|, \quad i = 1, 2, \dots, N. \quad (6)$$

DuLUT for Non-linear Functions. Lookup table (LUT) is commonly used for integer inference of non-linear functions in quantized neural networks. Linear LUT can compute functions losslessly when the input quantization bit width is less than or equal to the number of LUT entries. However, for higher-bit inputs, conventional linear LUT become impractical due to exponentially increasing table sizes—requiring 256 entries for 8-bit inputs and 65,536 entries for 16-bit inputs—leading to significant storage and computational overhead.

To improve precision without excessive resource usage, non-linear LUT have been proposed. These methods allocate more entries to regions where the function changes rapidly and fewer entries where it remains flat, thus enhancing quantization precision in critical areas. However, non-linear LUT are complex to implement in hardware, necessitating additional processing to define input regions based on function characteristics, and are not efficiently supported by most hardware architectures. Approximation methods like I-BERT [18] and I-ViT [22] attempt to simplify computations but introduce approximation errors and increased

computational steps, offsetting the benefits of quantization.

To address these challenges, we propose DuLUT, which uses two small linear tables tailored to the function’s properties, enabling accurate non-linear approximation with significantly reduced table sizes. DuLUT splits the input domain into two regions—typically where the function is rapidly changing and where it is relatively flat—and employs a separate small linear LUT for each region. For example, with 8-bit quantization, DuLUT uses two tables of 32 entries each without compromising precision (see Fig.7 and Algorithm 2). We applied DuLUT to common activation functions like softmax, GELU, and SiLU. By utilizing DuLUT, we achieve the same precision as larger single-table lookups while significantly reducing SRAM overhead and maintaining computational efficiency.

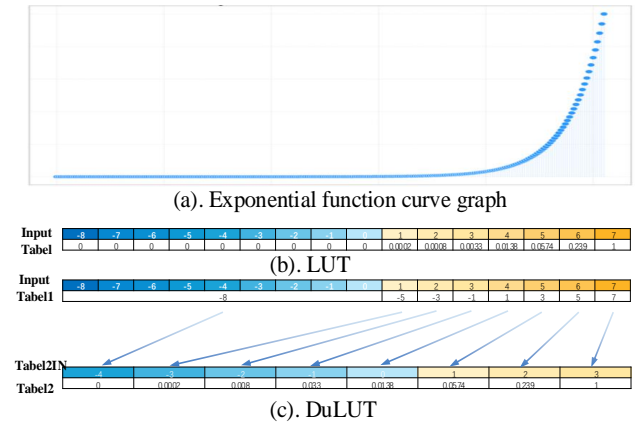


Figure 7. Illustration for LUT and DuLUT

Algorithm 2: Pseudo-code of DuLUT.

```
1 For a nonlinear function  $f$ : Determine segmentation points based
  on the curvature of  $f$ ;
2 Partition the input domain into shrink, enlarge, and unchanged
  regions;
3 Compress the shrink region’s table entries into one, reallocating
  saved entries to the enlarge region;
4 As an illustrative example, construct table1 and table2, each
  with 32 entries for 8-bit input (int8);
5 for each quantized input  $i_x$  do
6   Compute the index:
7    $i_x = i_x + 128$ ;
8    $\text{index} = ((\text{table1}[i_x[0:5]] \times (8 - i_x[5:]) +$ 
      $\text{table1}[i_x[0:5] + 1] \times i_x[5:] + (1 \ll 2)) \gg 3) + 128$ ;
9   Compute the quantized output:
      $\text{out} = (\text{table2}[\text{index}[0:5]] \times (8 - \text{index}[5:] +$ 
      $\text{table2}[\text{index}[0:5] + 1] \times \text{index}[5:]) \div 8$ ;
10 end
11 Return: out;
```

4. Experiment

4.1. Experimental Setup

Benchmark. We use the nuScenes dataset, a comprehensive autonomous driving dataset covering object detection, tracking, and LiDAR segmentation. The vehicle is equipped with one LiDAR, five radars, and six cameras providing a 360-degree view. The dataset comprises 1,000 driving scenes split into training (700 scenes), validation (150 scenes), and testing (150 scenes) subsets. Each scene lasts 20 seconds, annotated at 2 Hz.

Metrics. Following the official evaluation protocol, we report the nuScenes Score (NDS), mean Average Precision (mAP), and five true positive metrics: mean Average Translation Error (mATE), Scale Error (mASE), Orientation Error (mAOE), Velocity Error (mAVE), and Attribute Error (mAAE).

Experimental Details. Our experiments encompass both floating-point training and quantization configurations. For floating-point training, we follow PETR series settings, using PETR with an R50dcn backbone unless specified, and utilize the C5 feature (1/32 resolution output) as the 2D feature. Input images are at 1408×512 resolution. Both the lidar-ray PE and QD-aware lidar-ray PE use a pixel-wise depth of 30m with three anchor embeddings per axis. The 3D perception space is defined as $[-61.2, 61.2]$ m along the X and Y axes, and $[-10, 10]$ m along the Z axis. We also compare these positional encodings on StreamPETR, using a V2-99 backbone and input images of 800×320 resolution.

Training uses the AdamW optimizer (weight decay 0.01) with an initial learning rate of 2.0×10^{-4} , decayed via a cosine annealing schedule. We train for 24 epochs with a batch size of 8 on four NVIDIA RTX 4090 GPUs. No test-time augmentation is applied.

For quantization, we adopt 8-bit symmetric per-tensor

post-training quantization, using 32 randomly selected training images for calibration. When quantizing the scaled dot-product in cross-attention, we define a candidate set of 20 scaling factors.

4.2. Ablation Study

Proof of Position Encoding Equivalence We conducted experiments to verify whether the proposed QD-aware lidar-ray PE enhances floating-point performance over the original camera-ray PE. As shown in Tab. 2, QD-aware lidar-ray PE provides performance improvements. On PETR, it slightly increases mAP by 0.07 but significantly boosts NDS and mATE by 1.09 and 1.67, respectively. For Stream-PETR, our method yields substantial and balanced enhancements, with increases of 0.94 in mAP, 0.46 in NDS, and 0.22 in mATE.

Method		mAP \uparrow	NDS \uparrow	mATE \downarrow
PETR	Camera-ray PE	31.42	36.11	84.19
	QD-aware lidar-ray PE	31.49(0.07)	37.20(1.09)	82.52(1.67)
Stream-PETR	Camera-ray PE	48.19	57.11	60.99
	QD-aware lidar-ray PE	49.13(0.94)	57.57(0.46)	60.77(0.22)

Table 2. Floating-Point Performance Comparison of different 3D position embedding.

Effect of Anchor Embedding Quantity. The QD-aware lidar-ray PE uses three anchor embeddings per axis, obtained through linear interpolation. Experiments (Tab. 3) demonstrate that setting the number of anchor embeddings to 3 achieves the highest NDS and mAP scores. Adjusting this number either up or down results in lower performance, confirming that 3 is the optimal choice.

Quantity of Anchor Embedding			NDS \uparrow	mAP \uparrow
x-axis	y-axis	z-axis		
2	2	2	36.66	31.29
3	3	3	37.20	31.49
4	4	4	36.92	31.09
5	5	5	36.83	31.19

Table 3. Effect of Anchor Embedding Quantity.

Quantization Performance of Different Position Encodings To experimentally demonstrate the superior quantization performance of our proposed QD-aware lidar-ray PE, we focus solely on quantizing the positional encoding, keeping all other modules in floating-point computation. Detailed results are shown in Tab.4. The original camera-ray configuration loses up to 11.97% in mAP and 5.04% in NDS, whereas our QD-aware lidar-ray PE experiences minimal losses of only **1.42%** in mAP and **1.15%** in NDS. Figure8 further supports this finding; compared to the distribution in Fig. 3, the distribution of our QD-aware

lidar-ray PE aligns more closely with that of image features, retaining sufficient useful information.

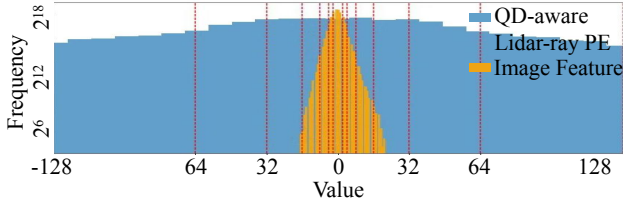


Figure 8. Illustration for distributions of image features and QD-aware lidar-ray PE after symmetric quantization using the quantization parameters derived from the respectively 3D-aware K.

Method		NDS↑	mAP↑	mATE↓
PETR	Camera-ray PE	34.29	27.66	87.17
	QD-aware lidar-ray PE	36.77	31.04	82.92
Stream-PETR	Camera-ray PE	53.74	40.23	69.39
	QD-aware lidar-ray PE	56.81	47.65	61.53

Table 4. Quantization Performance Comparison of different 3D position embedding.

Impact of Different Scaled Dot Product Quantization Strategy. To validate our novel scaled dot-product quantization strategy—which searches for the optimal scaling factor by minimizing softmax output error—we focus solely on quantizing the softmax inputs while keeping all other modules in floating-point computation. As shown in Tab. 5, the original quantization strategy results in significant losses of 40% in NDS and 50% in mAP. In contrast, our “quant after stabilization” approach greatly improves performance. An ablation study on the maximum candidate truncation range N reveals that setting $N \geq 20$ yields optimal quantization performance with nearly no loss. Performance deteriorates when $N < 20$ due to increased truncation of feature information, while values of N exceeding 20 offer no additional benefits. Therefore, setting $N = 20$ is sufficient to achieve the best performance.

Method		NDS↑	mAP↑	mATE↓
quant before stabilization	-	25.31	13.79	107.94
quant after stabilization	N = 1	3.45	1.23	150.34
	N = 5	33.86	28.77	87.12
	N = 10	34.65	29.33	85.01
	N = 20	36.10	31.42	84.19
	N = 30	36.10	31.42	84.19
	N = 40	36.10	31.42	84.19

Table 5. Performance of Different Scaled Dot Product Quantization Strategies.

Superior Performance of DuLUT for Non-linear Functions. To validate the quantization advantages of our proposed DuLUT for nonlinear functions, we use “quant

after stabilization ($N=20$)” from Tab. 5 as a baseline and evaluate the performance with different nonlinear function quantization methods applied on top of it. The specific results are shown in Tab. 7. We consider the carefully designed approximation methods I-Bert and I-Vit for different nonlinear functions. Due to the approximation errors introduced by these methods, many points are quantized away. Additionally, we compare with the LUT-based table lookup method and find that 256 entries are required for lossless quantization, while 128 entries lead to severe performance losses of 0.54 NDS and 0.37 mAP. In contrast, our newly proposed DuLUT with 128 entries achieves lossless quantization. Even when the number of entries is further reduced to 64, the quantization only results in a negligible loss of 0.08% NDS and 0.02% mAP, which can be considered negligible. This further demonstrates the superior quantization performance of our proposed DuLUT.

4.3. Validation on PETR-series Methods

We evaluate the effectiveness of our proposed method on various PETR-series models from both floating-point and quantized performance perspectives, specifically considering single-frame PETR and temporal multi-frame Stream-PETR models.

First, we analyze changes in floating-point performance (values in parentheses in Tab. 6). In single-frame PETR models, mAP and NDS generally improve across configurations, except for a slight decrease of 0.06 in NDS when using V2-99’s P4 feature with 640×1600 resolution images. mAP increases range from 0.07 to 0.69, while NDS shows significant gains in all cases, ranging from 0.87 to 1.24. For temporal multi-frame StreamPETR models, both mAP and NDS consistently improve, with mAP gains of 0.93 and 0.94, and modest NDS increases of 0.46 and 0.58. Notably, NDS improvements in temporal methods are smaller than in single-frame methods, mainly due to performance degradation in mASE and mAOE, suggesting that our QD-aware lidar-ray PE may not optimally capture scale and orientation information in temporal models. We plan to investigate this further in future work. Overall, QPETR shows significant improvements in most configuration metrics, demonstrating that our method surpasses the original PETR models in floating-point performance.

Next, we analyze the quantized performance improvements (values in square brackets in Table 6). In single-frame PETR models, mAP and NDS drops are kept below 1% using our QD-aware lidar-ray PE and smoothing techniques. In temporal multi-frame StreamPETR models, mAP and NDS drops remain within 2.5%, likely due to accumulated quantization errors during temporal fusion. Overall, quantized QPETR models maintain high performance with minimal drops in both settings, demonstrating the effectiveness of our quantization strategies in preserv-

Table 6. Comparison of floating-point and quantization Performance on PETR-series methods [29, 30, 49]. Red and blue text in the parentheses denote floating-point improvement and degradation respectively for our models compared to original PETR-series. We use the performance loss percentage to measure the gap between quantized performance and original floating-point performance, the red and blue text in the square brackets denote quantization improvement and degradation compared to respectively floating-point performance.

Backbone	Input Size	Feature	Mode	mAP \uparrow	NDS \uparrow	mATE \downarrow	mASE \downarrow	mAOE \downarrow	mAVE \downarrow	mAAE \downarrow	
R50*	512 \times 1408	c5	PETR	FP32	31.42	36.11	84.19	28.42	60.69	99.08	23.58
				PTQ	13.79[56.11]	25.31[29.91]	107.94[28.21]	31.47[10.73]	75.22[23.94]	83.71[15.51]	25.45[7.93]
			Q-PETR	FP32	31.49(0.07)	37.20(1.09)	82.52(1.67)	27.88(0.54)	59.91(0.78)	91.74(7.34)	23.45(0.13)
				PTQ	31.34[0.47]	37.17[0.82]	82.61[0.65]	27.93[0.17]	60.00[0.15]	91.79[0.00]	23.45[0.00]
R50*	512 \times 1408	p4	PETR	FP32	32.60	37.16	82.63	27.96	61.06	95.81	23.91
				PTQ	12.97[60.21]	24.75[33.39]	108.28[31.04]	31.76[13.59]	79.57[30.31]	78.90[17.65]	27.14[13.51]
			Q-PETR	FP32	32.69(0.09)	38.03(0.87)	80.58(2.05)	27.89(0.07)	59.43(0.63)	92.69(3.12)	22.55(1.36)
				PTQ	32.40[0.88]	37.72[0.82]	81.11[0.65]	27.92[0.10]	60.02[0.97]	92.76[0.00]	22.59[0.18]
R101*	512 \times 1408	p4	PETR	FP32	34.40	38.62	80.67	28.03	57.13	95.74	24.20
				PTQ	13.53[60.67]	23.84[38.27]	111.04[37.65]	31.27[11.56]	78.94[38.18]	92.92[2.95]	26.14[8.02]
			Q-PETR	FP32	34.72(0.32)	39.68(1.06)	79.40(1.27)	27.92(0.11)	53.90(3.23)	92.99(2.75)	22.59(1.61)
				PTQ	34.41[0.89]	39.08[1.51]	80.98[1.98]	28.00[0.28]	54.41[0.94]	92.62[0.39]	22.59[0.47]
V2-99*	320 \times 800	p4	PETR	FP32	38.01	42.56	75.79	26.84	50.58	90.13	21.07
				PTQ	10.46[72.48]	23.64[44.45]	112.41[36.21]	33.00[22.95]	85.96[69.95]	71.83[20.30]	25.12[19.22]
			Q-PETR	FP32	38.43(0.42)	43.80(1.24)	74.79(1.00)	27.29(0.45)	49.76(0.82)	82.11(8.02)	20.15(0.92)
				PTQ	37.93[1.30]	43.17[1.44]	75.50[0.94]	27.78[1.79]	50.07[0.62]	82.41[0.36]	20.38[1.14]
V2-99*	640 \times 1600	p4	PETR	FP32	40.66	46.05	71.76	27.07	42.23	80.68	21.06
				PTQ	6.40[84.63]	20.98[54.55]	117.38[33.22]	34.85[25.92]	83.38[97.44]	76.83[4.79]	27.10[28.67]
			Q-PETR	FP32	41.35(0.69)	45.99(0.06)	72.18(0.42)	26.91(0.15)	45.05(2.82)	82.03(2.35)	20.67(0.39)
				PTQ	40.95[0.96]	45.64[1.09]	73.40[1.69]	27.05[0.52]	45.61[1.24]	82.17[0.17]	20.68[0.00]
V2-99*	320 \times 800	p4	StreamPETR	FP32	48.19	57.11	60.99	25.58	37.54	26.28	19.43
				PTQ	18.52(61.19)	36.47(36.11)	76.39(25.25)	31.44(22.90)	47.03(25.27)	30.22(14.99)	20.99(8.03)
			Q-StreamPETR	FP32	49.13(0.94)	57.57(0.46)	60.77(0.22)	26.14(0.56)	39.05(1.49)	24.81(1.47)	19.15(0.28)
				PTQ	48.21(1.87)	56.33(2.15)	63.00(3.66)	26.35(0.80)	39.17(0.31)	24.90(0.36)	19.19(0.21)
V2-99*	640 \times 1600	p4	StreamPETR	FP32	49.51	58.03	60.10	26.07	35.65	25.91	19.60
				PTQ	18.72(62.19)	35.66(38.54)	74.32(23.66)	30.39(16.76)	41.49(16.38)	30.53(17.83)	20.82(6.22)
			Q-StreamPETR	FP32	50.48(0.93)	58.61(0.58)	58.78(0.32)	26.16(0.09)	37.05(1.40)	25.69(0.22)	18.59(1.01)
				PTQ	49.44(2.06)	57.94(1.24)	60.30(2.52)	26.55(1.49)	37.07(0.00)	25.87(0.31)	18.59(0.00)

Method	NDS \uparrow	mAP \uparrow	mATE \downarrow
Quant after stabilization (N=20)	36.10	31.42	84.19
I-Bert	34.87	29.34	88.41
I-Vit	35.03	28.77	87.32
LUT	256 entries	36.10	31.42
	128 entries	35.56	31.05
DuLUT	(16,16) entries	28.12	17.36
	(16,32) entries	34.14	27.29
	(32,32) entries	36.07	31.36
	(64,64) entries	36.10	31.42

Table 7. Performance comparison of different quantization methods for nonlinear functions.

ing accuracy while reducing computational and memory requirements. We intend to further mitigate quantization errors in temporal models through enhanced error correction or advanced quantization methods.

5. Limitations

Although our method incurs almost no quantization accuracy loss, users need to replace the camera-ray in the original PETR series with our proposed QD-aware lidar-ray. The only drawback is that this requires retraining. However, from the perspective of quantization deployment, this

retraining is beneficial, and the floating-point precision can even be improved.

6. Conclusion

In this paper, we address the significant performance drops of PETR models during quantization by identifying two main issues: the imbalance between positional encoding and image feature magnitudes, and uneven scalar dot-products in cross-attention. To resolve these, we introduce Q-PETR, a quantization-friendly positional encoding transformation that redesigns positional encoding and improves scalar dot-product quantization without sacrificing the original floating-point performance. Our experiments show that Q-PETR limits mAP and NDS drops to below 1% under standard 8-bit post-training quantization and even surpasses the original PETR in floating-point precision. Extensive tests across various PETR models demonstrate the method’s strong generalization and deployment suitability. Future work will explore quantization error propagation in multi-frame temporal models and develop advanced quantization strategies to further reduce precision loss in temporal settings.

References

- [1] Saleh Ashkboos, Maximilian L Croci, Marcelo Gennari do Nascimento, Torsten Hoefer, and James Hensman. Slicept: Compress large language models by deleting rows and columns. *arXiv preprint arXiv:2401.15024*, 2024.
- [2] Saleh Ashkboos, Amirkeivan Mohtashami, Maximilian L Croci, Bo Li, Pashmina Cameron, Martin Jaggi, Dan Alistarh, Torsten Hoefer, and James Hensman. Quarot: Outlier-free 4-bit inference in rotated llms. *arXiv preprint arXiv:2404.00456*, 2024.
- [3] Ron Banner, Yury Nahshan, and Daniel Soudry. Post training 4-bit quantization of convolutional networks for rapid-deployment. In *Advances in Neural Information Processing Systems 32: Annual Conference on Neural Information Processing Systems 2019, NeurIPS 2019, December 8-14, 2019, Vancouver, BC, Canada*, pages 7948–7956, 2019.
- [4] Yash Bhargat, Jinwon Lee, Markus Nagel, Tijmen Blankevoort, and Nojun Kwak. Lsq+: Improving low-bit quantization through learnable offsets and better initialization. In *Proceedings of the IEEE/CVF conference on computer vision and pattern recognition workshops*, pages 696–697, 2020.
- [5] Nicolas Carion, Francisco Massa, Gabriel Synnaeve, Nicolas Usunier, Alexander Kirillov, and Sergey Zagoruyko. End-to-end object detection with transformers. *ArXiv*, abs/2005.12872, 2020.
- [6] Jungwook Choi, Zhuo Wang, Swagath Venkataramani, Pierce I-Jen Chuang, Vijayalakshmi Srinivasan, and Kailash Gopalakrishnan. PACT: parameterized clipping activation for quantized neural networks. *CoRR*, abs/1805.06085, 2018.
- [7] Yoni Choukroun, Eli Kravchik, Fan Yang, and Pavel Kisilev. Low-bit quantization of neural networks for efficient inference. In *2019 IEEE/CVF International Conference on Computer Vision Workshops, ICCV Workshops 2019, Seoul, Korea (South), October 27-28, 2019*, pages 3009–3018. IEEE, 2019.
- [8] Xiangxiang Chu, Liang Li, and Bo Zhang. Make repvgg greater again: A quantization-aware approach. In *AAAI Conference on Artificial Intelligence*, 2022.
- [9] Xiaomeng Chu, Jiajun Deng, Guoliang You, Yifan Duan, Yao Li, and Yanyong Zhang. Rayformer: Improving query-based multi-camera 3d object detection via ray-centric strategies. *arXiv preprint arXiv:2407.14923*, 2024.
- [10] Steven K Esser, Jeffrey L McKinstry, Deepika Bablani, Rathinakumar Appuswamy, and Dharmendra S Modha. Learned step size quantization. *arXiv preprint arXiv:1902.08153*, 2019.
- [11] Suyog Gupta, Ankur Agrawal, K. Gopalakrishnan, and Pritish Narayanan. Deep learning with limited numerical precision. In *International Conference on Machine Learning*, 2015.
- [12] Philipp Gysel, Jon J. Pimentel, Mohammad Motamedi, and Soheil Ghiasi. Ristretto: A framework for empirical study of resource-efficient inference in convolutional neural networks. *IEEE Transactions on Neural Networks and Learning Systems*, 29:5784–5789, 2018.
- [13] Hai Victor Habi, Reuven Peretz, Elad Cohen, Lior Dikstein, Oranit Dror, Idit Diamant, Roy H. Jennings, and Arnon Netzer. Hptq: Hardware-friendly post training quantization. *ArXiv*, abs/2109.09113, 2021.
- [14] Jinghua Hou, Tong Wang, Xiaoqing Ye, Zhe Liu, Shi Gong, Xiao Tan, Errui Ding, Jingdong Wang, and Xiang Bai. Open: Object-wise position embedding for multi-view 3d object detection. *arXiv preprint arXiv:2407.10753*, 2024.
- [15] Andrew G. Howard, Menglong Zhu, Bo Chen, Dmitry Kalenichenko, Weijun Wang, Tobias Weyand, Marco Andreetto, and Hartwig Adam. Mobilenets: Efficient convolutional neural networks for mobile vision applications. *ArXiv*, abs/1704.04861, 2017.
- [16] Huang Junjie and Huang Guan. Bevdet4d: Exploit temporal cues in multi-camera 3d object detection. *arXiv preprint arXiv:2203.17054*, 2022.
- [17] Huang Junjie, Huang Guan, Zhu Zheng, and Du Dalong. Bevdet: High-performance multi-camera 3d object detection in bird-eye-view. *arXiv preprint arXiv:2112.11790*, 2021.
- [18] Sehoon Kim, Amir Gholami, Zhewei Yao, Michael W Mahoney, and Kurt Keutzer. I-bert: Integer-only bert quantization. In *International conference on machine learning*, pages 5506–5518. PMLR, 2021.
- [19] Hao Li, Asim Kadav, Igor Durdanovic, Hanan Samet, and Hans Peter Graf. Pruning filters for efficient convnets. *ArXiv*, abs/1608.08710, 2016.
- [20] Peng Li, Chang Shu, Yuan Xie, Yan Qu, and Hui Kong. Hierarchical knowledge squeezed adversarial network compression. In *AAAI Conference on Artificial Intelligence*, 2020.
- [21] Yuhang Li, Ruihao Gong, Xu Tan, Yang Yang, Peng Hu, Qi Zhang, Fengwei Yu, Wei Wang, and Shi Gu. Brecq: Pushing the limit of post-training quantization by block reconstruction. In *International Conference on Learning Representations*, 2021.
- [22] Zhikai Li and Qingyi Gu. I-vit: Integer-only quantization for efficient vision transformer inference. In *Proceedings of the IEEE/CVF International Conference on Computer Vision*, pages 17065–17075, 2023.
- [23] Zhiqi Li, Wenhai Wang, Hongyang Li, Enze Xie, Chonghao Sima, Tong Lu, Qiao Yu, and Jifeng Dai. Bevformer: Learning bird’s-eye-view representation from multi-camera images via spatiotemporal transformers. *arXiv preprint arXiv:2203.17270*, 2022.
- [24] Zhikai Li, Junrui Xiao, Lianwei Yang, and Qingyi Gu. Repqvit: Scale reparameterization for post-training quantization of vision transformers. In *Proceedings of the IEEE/CVF International Conference on Computer Vision*, pages 17227–17236, 2023.
- [25] Xuewu Lin, Tianwei Lin, Zixiang Pei, Lichao Huang, and Zhizhong Su. Sparse4d: Multi-view 3d object detection with sparse spatial-temporal fusion. *arXiv preprint arXiv:2211.10581*, 2022.
- [26] Yang Lin, Tianyu Zhang, Peiqin Sun, Zheng Li, and Shuchang Zhou. Fq-vit: Post-training quantization for fully quantized vision transformer. *arXiv preprint arXiv:2111.13824*, 2021.

- [27] Hanxiao Liu, Karen Simonyan, and Yiming Yang. Darts: Differentiable architecture search. *ArXiv*, abs/1806.09055, 2018.
- [28] Haisong Liu, Yao Teng, Tao Lu, Haiguang Wang, and Liming Wang. Sparsebev: High-performance sparse 3d object detection from multi-camera videos. *2023 IEEE/CVF International Conference on Computer Vision (ICCV)*, pages 18534–18544, 2023.
- [29] Yingfei Liu, Tiancai Wang, Xiangyu Zhang, and Jian Sun. Petr: Position embedding transformation for multi-view 3d object detection. *arXiv preprint arXiv:2203.05625*, 2022.
- [30] Yingfei Liu, Junjie Yan, Fan Jia, Shuailin Li, Qi Gao, Tiancai Wang, Xiangyu Zhang, and Jian Sun. Petr2: A unified framework for 3d perception from multi-camera images. *arXiv preprint arXiv:2206.01256*, 2022.
- [31] Zhijian Liu, Haotian Tang, Alexander Amini, Xinyu Yang, Huizi Mao, Daniela Rus, and Song Han. Bevfusion: Multi-task multi-sensor fusion with unified bird’s-eye view representation. *arXiv preprint arXiv:2205.13542*, 2022.
- [32] Zechun Liu, Changsheng Zhao, Igor Fedorov, Bilge Soran, Dhruv Choudhary, Raghuraman Krishnamoorthi, Vikas Chandra, Yuandong Tian, and Tijmen Blankevoort. Spinquant-llm quantization with learned rotations. *arXiv preprint arXiv:2405.16406*, 2024.
- [33] Markus Nagel, Mart van Baalen, Tijmen Blankevoort, and Max Welling. Data-free quantization through weight equalization and bias correction. In *Proceedings of the IEEE/CVF International Conference on Computer Vision*, pages 1325–1334, 2019.
- [34] Markus Nagel, Rana Ali Amjad, Mart Van Baalen, Christos Louizos, and Tijmen Blankevoort. Up or down? adaptive rounding for post-training quantization. In *International Conference on Machine Learning*, pages 7197–7206. PMLR, 2020.
- [35] Daniele Jahier Pagliari, Matteo Risso, Beatrice Alessandra Motetti, and Alessio Burrello. Plinio: a user-friendly library of gradient-based methods for complexity-aware dnn optimization. In *2023 Forum on Specification & Design Languages (FDL)*, pages 1–8. IEEE, 2023.
- [36] Nilesh Prasad Pandey, Markus Nagel, Mart van Baalen, Yin Huang, Chirag Patel, and Tijmen Blankevoort. A practical mixed precision algorithm for post-training quantization. *arXiv preprint arXiv:2302.05397*, 2023.
- [37] Jonah Philion and Sanja Fidler. Lift, splat, shoot: Encoding images from arbitrary camera rigs by implicitly unprojecting to 3d. In *ECCV*, 2020.
- [38] Mark Sandler, Andrew G. Howard, Menglong Zhu, Andrey Zhmoginov, and Liang-Chieh Chen. Mobilenetv2: Inverted residuals and linear bottlenecks. *2018 IEEE/CVF Conference on Computer Vision and Pattern Recognition*, pages 4510–4520, 2018.
- [39] Wenqi Shao, Mengzhao Chen, Zhaoyang Zhang, Peng Xu, Lirui Zhao, Zhiqian Li, Kaipeng Zhang, Peng Gao, Yu Qiao, and Ping Luo. Omniquant: Omnidirectionally calibrated quantization for large language models. *arXiv preprint arXiv:2308.13137*, 2023.
- [40] Tao Sheng, Chen Feng, Shaojie Zhuo, Xiaopeng Zhang, Liang Shen, and Mickey Aleksic. A quantization-friendly separable convolution for mobilenets. *2018 1st Workshop on Energy Efficient Machine Learning and Cognitive Computing for Embedded Applications (EMC2)*, pages 14–18, 2018.
- [41] Huihong Shi, Xin Cheng, Wendong Mao, and Zhongfeng Wang. P2-vit: Power-of-two post-training quantization and acceleration for fully quantized vision transformer. *arXiv preprint arXiv:2405.19915*, 2024.
- [42] Changyong Shu, Yifan Liu, Jianfei Gao, Zheng Yan, and Chunhua Shen. Channel-wise knowledge distillation for dense prediction*. *2021 IEEE/CVF International Conference on Computer Vision (ICCV)*, pages 5291–5300, 2020.
- [43] Changyong Shu, Jiajun Deng, Fisher Yu, and Yifan Liu. 3dppe: 3d point positional encoding for multi-camera 3d object detection transformers. *arXiv preprint arXiv:2211.14710*, 2023.
- [44] Yu-Shan Tai, Ming-Guang Lin, and An-Yeu Andy Wu. Tsptq-vit: Two-scaled post-training quantization for vision transformer. In *ICASSP 2023-2023 IEEE International Conference on Acoustics, Speech and Signal Processing (ICASSP)*, pages 1–5. IEEE, 2023.
- [45] Mingxing Tan and Quoc V. Le. Efficientnet: Rethinking model scaling for convolutional neural networks. *ArXiv*, abs/1905.11946, 2019.
- [46] Min Wang, Baoyuan Liu, and Hassan Foroosh. Look-up table unit activation function for deep convolutional neural networks. In *2018 IEEE Winter Conference on Applications of Computer Vision (WACV)*, pages 1225–1233. IEEE, 2018.
- [47] Runqi Wang, Huixin Sun, Linlin Yang, Shaohui Lin, Chuanjian Liu, Yan Gao, Yao Hu, and Baochang Zhang. Aq-detr: Low-bit quantized detection transformer with auxiliary queries. In *Proceedings of the AAAI Conference on Artificial Intelligence*, pages 15598–15606, 2024.
- [48] Shihao Wang, Xiaohui Jiang, and Ying Li. Focal-petr: Embracing foreground for efficient multi-camera 3d object detection. *arXiv preprint arXiv:2212.05505*, 2022.
- [49] Shihao Wang, Yingfei Liu, Tiancai Wang, Ying Li, and Xiangyu Zhang. Exploring object-centric temporal modeling for efficient multi-view 3d object detection. In *Proceedings of the IEEE/CVF International Conference on Computer Vision*, pages 3621–3631, 2023.
- [50] Shihao Wang, Zhiding Yu, Xiaohui Jiang, Shiyi Lan, Min Shi, Nadine Chang, Jan Kautz, Ying Li, and Jose M Alvarez. Omnidrive: A holistic llm-agent framework for autonomous driving with 3d perception, reasoning and planning. *arXiv preprint arXiv:2405.01533*, 2024.
- [51] Yue Wang, Vitor Campagnolo Guizilini, Tianyuan Zhang, Yilun Wang, Hang Zhao, and Justin Solomon. Detr3d: 3d object detection from multi-view images via 3d-to-2d queries. In *Conference on Robot Learning*, pages 180–191. PMLR, 2022.
- [52] Zitian Wang, Zehao Huang, Jiahui Fu, Naiyan Wang, and Si Liu. Object as query: Lifting any 2d object detector to 3d detection. In *Proceedings of the IEEE/CVF International Conference on Computer Vision*, pages 3791–3800, 2023.
- [53] Xiuying Wei, Yunchen Zhang, Xiangguo Zhang, Ruihao Gong, Shanghang Zhang, Qi Zhang, Fengwei Yu, and Xianglong Liu. Outlier suppression: Pushing the limit of low-bit

- transformer language models. *Advances in Neural Information Processing Systems*, 35:17402–17414, 2022.
- [54] Guangxuan Xiao, Ji Lin, Mickael Seznec, Hao Wu, Julien Demouth, and Song Han. Smoothquant: Accurate and efficient post-training quantization for large language models. In *International Conference on Machine Learning*, pages 38087–38099. PMLR, 2023.
- [55] Sheng Xu, Yanjing Li, Mingbao Lin, Peng Gao, Guodong Guo, Jinhu Lü, and Baochang Zhang. Q-detr: An efficient low-bit quantized detection transformer. In *Proceedings of the IEEE/CVF Conference on Computer Vision and Pattern Recognition*, pages 3842–3851, 2023.
- [56] Junjie Yan, Yingfei Liu, Jianjian Sun, Fan Jia, Shuailin Li, Tiancai Wang, and Xiangyu Zhang. Cross modal transformer via coordinates encoding for 3d object detection. *arXiv preprint arXiv:2301.01283*, 2023.
- [57] Yuewei Yang, Xiaoliang Dai, Jialiang Wang, Peizhao Zhang, and Hongbo Zhang. Efficient quantization strategies for latent diffusion models. *arXiv preprint arXiv:2312.05431*, 2023.
- [58] Tianwei Yin, Xingyi Zhou, and Philipp Krähenbühl. Center-based 3D Object Detection and Tracking. *arXiv preprint arXiv:2006.11275*, 2020.
- [59] Li Yin hao, Ge Zheng, Yu Guanyi, Yang Jinrong, Wang Zengran, Shi Yukang, Sun Jianjian, and Li Zeming. Bevdepth: Acquisition of reliable depth for multi-view 3d object detection. *arXiv preprint arXiv:2206.10092*, 2022.
- [60] Zichen Yu and Changyong Shu. Ultimatedo: An efficient framework to marry occupancy prediction with 3d object detection via channel2height. *arXiv preprint arXiv:2409.11160*, 2024.
- [61] Zichen Yu, Changyong Shu, Jiajun Deng, Kangjie Lu, Zongdai Liu, Jiangyong Yu, Dawei Yang, Hui Li, and Yan Chen. Flashocc: Fast and memory-efficient occupancy prediction via channel-to-height plugin. 2023.
- [62] Zichen Yu, Changyong Shu, Qianpu Sun, Junjie Linghu, Xiaobao Wei, Jiangyong Yu, Zongdai Liu, Dawei Yang, Hui Li, and Yan Chen. Panoptic-flashocc: An efficient baseline to marry semantic occupancy with panoptic via instance center. *arXiv preprint arXiv:2406.10527*, 2024.
- [63] Zhihang Yuan, Chenhao Xue, Yiqi Chen, Qiang Wu, and Guangyu Sun. Ptq4vit: Post-training quantization for vision transformers with twin uniform quantization. In *European conference on computer vision*, pages 191–207. Springer, 2022.
- [64] Stone Yun and Alexander Wong. Do all mobilenets quantize poorly? gaining insights into the effect of quantization on depthwise separable convolutional networks through the eyes of multi-scale distributional dynamics. *2021 IEEE/CVF Conference on Computer Vision and Pattern Recognition Workshops (CVPRW)*, pages 2447–2456, 2021.
- [65] Dongqing Zhang, Jiaolong Yang, Dongqiangzi Ye, and Gang Hua. Lq-nets: Learned quantization for highly accurate and compact deep neural networks. In *Computer Vision - ECCV 2018 - 15th European Conference, Munich, Germany, September 8-14, 2018, Proceedings, Part VIII*, pages 373–390. Springer, 2018.
- [66] Yifan Zhang, Zhen Dong, Huanrui Yang, Ming Lu, Cheng-Ching Tseng, Yuan Du, Kurt Keutzer, Li Du, and Shanghang Zhang. Qd-bev: quantization-aware view-guided distillation for multi-view 3d object detection. In *Proceedings of the IEEE/CVF International Conference on Computer Vision*, pages 3825–3835, 2023.
- [67] Li Zhiqi, Wang Wenhai, Li Hongyang, Xie Enze, Sima Chonghao, Lu Tong, Yu Qiao, and Dai Jifeng. Bevformer: Learning bird’s-eye-view representation from multi-camera images via spatiotemporal transformers. *arXiv preprint arXiv:2203.17270*, 2022.
- [68] Sifan Zhou, Liang Li, Xinyu Zhang, Bo Zhang, Shipeng Bai, Miao Sun, Ziyu Zhao, Xiaobo Lu, and Xiangxiang Chu. Lidar-ptq: Post-training quantization for point cloud 3d object detection. *arXiv preprint arXiv:2401.15865*, 2024.